Analysis of CO_2 spatiotemporal variations in China using ~~tower data and~~ a weather-biosphere-online-coupled model~~, WRF-VPRM~~

Xinyi Dong[1,2], Man Yue[1,2], Yujun Jiang[3,4], Xiao-Ming Hu[5], Qianli Ma[4], Jingjiao Pu[3], and Guangqiang Zhou[6]

[1]School of Atmospheric Science, Nanjing University, Nanjing, 210023, China
[2]Joint International Research Laboratory of Atmospheric and Earth System Sciences & Institute for Climate and Global Change Research, Nanjing University, Nanjing, 210023, China
[3]Zhejiang Meteorological Science Institute, Hangzhou 310008, China
[4]Zhejiang Lin'an Atmospheric Background National Observation and Research Station, Hangzhou 311307, China
[5]Center for Analysis and Prediction of Storms, University of Oklahoma, Norman, Oklahoma, 73072, USA
[6]Shanghai Key Laboratory of Health and Meteorology, Shanghai Meteorological Service, Shanghai, 200135, China

Correspondence to: Yujun Jiang (yjjiang@pku.org.cn) and Xiao-Ming Hu (xhu@ou.edu)

Abstract. Dynamics of atmospheric CO_2 has received considerable attention in the literature, yet significant uncertainties remain within the estimates of contribution from terrestrial flux and the influence of atmospheric mixing. In this study we apply the Weather Research and Forecasting model coupled with Vegetation Photosynthesis and Respiration Model (WRF-VPRM) in China to characterize ~~CO_2~~the dynamics ~~with tower data collected at a background site Lin'an (30.30°N, 119.75°E).~~of CO_2 in the atmosphere. The online coupled ~~weather-biosphere~~ WRF-VPRM ~~simulations are~~is able to simulate biosphere processes (photosynthetic uptake and ecosystem respiration) and meteorology in one coordinate system. ~~Simulations are conducted for three years (2016-2018) with fine grid resolution (20 km) to detail the spatiotemporal variations of CO_2 fluxes and concentrations. This is the first attempt to apply the weather-biosphere model for a multi-year simulation~~We apply WRF-VPRM for a multi-year simulation (2016-2018) with integrated data from a satellite product, flask samplings, and tower measurements to diagnose the ~~dynamics~~spatiotemporal variations of CO_2 ~~in~~ fluxes and concentrations in China. We find that the spatial distribution of CO_2 ~~is determined~~was dominated by anthropogenic emissions, while its seasonality (with ~~maximum concentrations~~maxima in April 15 ppmv higher than ~~minimums~~minima in August) ~~is~~was dominated by terrestrial flux and background CO_2. Observations and simulations ~~reveal~~revealed a consistent increasing trend in column-averaged CO_2 (XCO_2) of 2.46 ppmv (0.6%/yr) resulting from anthropogenic emission growth and biosphere uptake. WRF-VPRM successfully ~~reproduces~~reproduced ground-based measurements of surface CO_2 concentration with mean bias of -0.79 ppmv ~~(-0.20%)~~ and satellite derived XCO_2 with mean bias of 0.76 ppmv ~~(0.19%).~~ The model-simulated seasonality ~~is~~was also consistent with observations, with correlation coefficients of 0.90 and 0.89 for ground-based measurements and ~~Orbiting Carbon Observatory-2 (OCO-2)~~ satellite data, respectively. ~~However, evaluation against Lin'an tower data reveals uncertainty within the model for simulating the intensity and diurnal variation of terrestrial flux, which contributes to overestimation by ~5.35 ppmv (1.26%).~~

~~Lin'an tower~~Tower observations ~~also reveal~~from a background site Lin'an (30.30°N, 119.75°E) revealed a strong correlation (-0.~~85~~98) between vertical CO_2 and temperature gradients, suggesting a significant influence of boundary layer thermal structure on the accumulation and depletion of atmospheric CO_2.

1 Introduction

Climate research requires accurate characterization of atmospheric CO_2, which is closely affected by the both atmospheric transport and terrestrial sources and sinks (Bauska et al., 2015; Keenan et al., 2016). Our current knowledge largely comes from interpreting ground- or space-based measurements and model simulations. While observation is limited by spatial and temporal coverages, modelling approaches also suffer from various uncertainties (Shi et al., 2018). Modelling assessment of CO_2 is usually conducted through two methods: first, process- or data-driven biosphere models in which terrestrial fluxes are diagnostically calculated with theoretical functions (Tian et al., 2015) or determined through semi-empirical relationships derived from ground measurements and/or satellite products with machine learning techniques (Papale and Valentini, 2003); second, inverse modelling in which prior flux estimates applied in atmospheric transport models are ~~calibrated by observational data and/or satellite products to determine posterior terrestrial flux (Peylin et al., 2002).~~adjusted by observational data and/or satellite products to determine posterior flux (Peylin et al., 2002;Kountouris et al., 2018). Process-driven biosphere models have difficulties capturing spatial and temporal variabilities at fine resolution because parameters calibrated from a limited number of site observations are applied across a variety of land covers (Todd-Brown et al., 2013). Atmospheric inverse modelling is predominantly affected by the presumed prior flux, and different assimilation techniques can give different and even conflicting results (Peylin et al., 2013). These fundamental features highlight the limits of these approaches for accurately modelling carbon dynamics.

Researchers have attempted to reconcile differences between "bottom-up" biosphere models and "top-down" atmospheric inverse models, and recent studies have demonstrated increasing levels of agreement owing to improved understanding of both approaches, such as better parameterization of biosphere processes (Dayalu et al., 2018), more accurately constrained estimates of prior flux (Crowell et al., 2018;Feng et al., 2019), and advanced measurement/satellite instruments that provide high quality data for assimilation (Gaubert et al., 2019); however, critical model disagreements still persist (Kondo et al., 2020). To bridge the gap between terrestrial flux and atmospheric mixing, a type of weather-biosphere coupled model (Ahmadov et al., 2007;Mahadevan et al., 2008) ~~was~~has been developed to simulate biosphere processes and meteorology conditions in one coordinate system, allowing their interactions to be properly addressed. A few case studies (Ahmadov et al., 2009;Kretschmer et al., 2012;Park et al., 2018) have demonstrated the potential advantages of coupled weather-biosphere models over pure biosphere/inverse models for short term (a few weeks) simulations, but whether the coupled model is able to reproduce the spatial distributions and temporal variations and subsequently estimate carbon fluxes at regional scales with high confidence remains a crucial issue to be addressed.

Understanding the spatiotemporal characteristics of atmospheric CO_2 is a key priority in China because of the central role it plays in regulating the climate and environment. In recent years, tremendous efforts have been made in China to control anthropogenic emissions from fossil fuel combustion for both air quality and climate mitigation purposes (Zheng et al., 2018). While the sources and sinks of air pollutants have been thoroughly examined and well documented (Huang et al., 2020), the dynamics of CO_2 at regional to national scales remain poorly understood due to lack of long-term observations and limited modelling studies (Han et al., 2020). Li et al. (2020) applied a weather-biosphere model with tower observations to analyse CO_2 fluxes and concentrations over mixed forest and rice paddy in northeast China, but the one-year simulation limits the attempt to investigate interannual CO_2 variation which is subject to substantial change (Fu et al., 2019b). Wang et al. (2019) applied satellite products and in-situ observations with inverse modelling to derive posterior carbon fluxes and reported 100% uncertainty for constraining global terrestrial flux. Fu et al. (2020) applied GEOS-Chem simulation with offline Carbon Tracker (Peters et al., 2007) as input to estimate impacts of terrestrial flux and anthropogenic emissions on the annual variation of CO_2 concentrations, but regional-scale assessment was limited by coarse grid resolution (2°×2.5°). Machine-learning technique has also been employed to upscale site observations to regional-scale (Yao et al., 2018; Zhu et al., 2014), but the estimations of carbon budget and dynamics retain large uncertainty due to the diversity of biomass among sites and ~~suffer from~~ coarse grid resolution. These pilot studies have shed light on improving the understanding of spatiotemporal characteristics of CO_2 in China with modelling or observational methods, but an integrated investigation with both modelling and observations at fine-scale is urgently needed to expand diagnostic understanding of localized and regional transport, flux, and concentration of CO_2 to inform emission management and climate adaption policies (Fu et al., 2019a;Niu et al., 2017;Wang et al., 2019).

In this study we ~~apply~~use the Weather Research and Forecasting model coupled with the Vegetation Photosynthesis and Respiration Model (WRF-VPRM) (Hu et al., 2020;Mahadevan et al., 2008) to simulate and characterize the spatiotemporal variation of atmospheric CO_2 in China from 2016-2018, and also to validate this weather-biosphere model with recent advanced satellite and tower observations. WRF-VPRM has been applied in a few case studies over the United States (Hu et al., 2020), Europe (Kretschmer et al., 2012), northeast China (Li et al., 2020), and South Korea (Park et al., 2020); this study ~~is the first~~ attempt to apply and evaluate it for a multi-year simulation ~~at fine scale (20 km)~~ over China. We first describe the modelling methods and data ~~employed~~ followed by model validation against observations from multiple datasets, and then present the spatiotemporal variations and estimates of contributions from anthropogenic emissions, terrestrial flux, and background concentrations. Finally, we ~~probe into~~investigate tower data and reveal the boundary layer thermal structure impacts on atmospheric CO_2 accumulation and depletion.

2 Method

~~The WRF-VPRM simulation in this study is configured with 48 vertical layers and 20 km grid resolution. Initial and boundary conditions are~~We conduct nested WRF(Version 3.9.1.1)-VPRM simulations over China (domain shown in Fig.1(a)) and Yangtze River Delta (YRD) region (domain shown in Fig.1(d)) at 20 km and 4 km grid resolution, respectively. Both

simulations were configured with 47 vertical layers with model tops at 10hPa. Model configuration in this study followed the work by Hu et al. (2020) and Li et al. (2020). We applied the YSU planetary boundary layer (PBL) scheme (Hong et al., 2006), Morrison microphysics (Morrison et al., 2009), Duhia short-wave radiation (Dudhia, 1989), RRTM long-wave radiation (Mlawer et al., 1997), Grell-3 cumulus scheme (Grell and Devenyi, 2002), and Noah land-surface scheme (Chen and Dudhia, 2001), with more details summarized in Table S1. In general, the 4km-grid simulation showed no significant difference as compared to the 20km-grid simulation (demonstrated in Figure S1 and Figure S2), thus the 20km-grid simulation was used to characterize the spatiotemporal distributions of CO_2 over China, and the 4km-grid simulation was only used to compare with tower data collected at a background site in YRD. Discussions in the next section will mostly refer to the 20km-grid simulation unless otherwise specified. Initial and lateral boundary conditions for the 20km-grid simulations were derived from the mole fraction product of CarbonTracker (Peters et al., 2007) with 3°×2° resolution. The latest update of column average CO_2 (XCO_2) concentration assimilation product from CarbonTracker (CT2019) with 1°×1° resolution ~~is~~(Jacobson, 2020) was also employed to compare with the WRF-VPRM simulation. The anthropogenic emission inventory is from the Open-source Data Inventory for Anthropogenic CO_2 (ODIAC) with 0.1°×0.1° resolution (Oda et al., 2018) shown in Fig.1(a); ocean flux is from climatology estimation (Takahashi et al., 2009); and vegetation fractions and enhanced vegetation index (EVI, shown in Fig.1(b)) are from MODIS (Huete et al., 2002). CO_2 from initial and boundary conditions, anthropogenic emission, and terrestrial biogenic flux ~~are~~were tagged as BCG, ANT, and BIO, respectively, to allow the contributions from each process to be identified and quantified through one simulation.

WRF-VPRM calculates ecosystem respiration (ER) and gross ecosystem exchange (GEE) with the following functions as:

$$ER = \alpha \times T + \beta \quad (1)$$

$$GEE = -\lambda \times T_{scale} \times W_{scale} \times P_{scale} \times (1 + PAR/PAR_0)^{-1} \times EVI \times PAR \quad (2)$$

where T is the air temperature at 2m above the surface (T2); α, β, λ are vegetation type-dependent parameters; PAR_0 is the vegetation type-dependent half-saturation value of photosynthetically active radiation (PAR); and $T_{scale}, W_{scale}, P_{scale}$ are scaling factors for temperature, water stress, and phenology, respectively. In this study we take the atmosphere as a reference, thus GEE has a negative sign and ER has a positive sign. The current version of WRF-VPRM is parameterized (α, β, λ) for 7 vegetation types (Fig.1(c)): crops, mixed forest, evergreen forest, deciduous forest, shrub, savanna, and grass. For each modelling grid, ER and GEE are calculated as the weighted averages of each vegetation type based on their fractional abundance. Recent studies~~–~~ (Hu et al., 2020;Li et al., 2020) have investigated the uncertainty associated with this parameterization through sensitivity simulations and suggested the crops can be further divided into subcategories based on eddy-covariance (EC) tower measurement to improve the model. In this study we ~~apply~~used the default parameterization~~,~~ (values presented in Table S2), which has been demonstrated to successfully reproduce the terrestrial flux over northeast China (Li et al., 2020). In contrast, CT2019 applies a ~~pure~~process based biosphere model, the Carnegie-Ames Stanford Approach (CASA(Zhou et al., 2020)), driven by year-specific weather and satellite data to simulate terrestrial fluxes (Peters et al., 2007). CASA also estimates photosynthetic uptake based on solar radiation and plant phenology, and estimates respiration as a

function of T2. CASA directly simulates monthly means of Net Primary Production (NPP) and heterotrophic respiration (R_H). NPP is the difference between photosynthetic uptake (equivalent to GEE) and autotrophic respiration (R_A). The summary of R_H and R_A is equivalent to ER. Thus, WRF-VPRM and CASA are essentially very similar in terms of considering methodology impact; however, it should be noted that to resolve CASA simulated NPP into GEE and R_A, CT2019 applies the assumption that GEE is twice that of NPP, which implies that for the same plants the photosynthetic carbon uptake is double the magnitude of autotrophic respiration (but of opposite sign). This assumption is applicable at monthly scale but may ~~contribute to~~ have difficulty ~~reproducing~~to reproduce the rapid changes at hourly and daily scales due to impact from weather systems, which will be demonstrated with more details in Section 3.2.

~~Measurements~~Hourly measurements of CO_2 concentrations ~~are~~were collected at the Lin'an Regional Atmospheric Background Station (30.30˚N, 119.75˚E, surroundings shown in Fig.~~1(d~~2(a)) with Picarro G1301 and G1302 trace gas analysers mounted on an observation tower at 21 and 55 meters, respectively, above ground level (AGL) and analysed online (data analysis lab shown in Fig.~~1(c~~2(b)). The station is located in the remote area of Hangzhou 138.6 meters above sea level in the middle of a hilly area covered by mixed forest. ~~The hourly Lin'an station tower measurements collected between 2016-2018 provide a representative sampling of the~~The observation tower is 60km to the west of downtown center of Hangzhou and 195km to the southwest of Shanghai. Fig.2(c) and (d) presents the wind rose map at Lin'an derived from hourly observations of 10m and 55m wind respectively, which clearly shows the northeast and southwest as prevailing wind directions. The station can properly represent the background atmospheric environment in YRD as demonstrated in previous studies (Deng et al., 2018;Pu et al., 2020). The tower data provides a representative sampling of CO_2 gradients resulting from exchange between atmosphere mixing and terrestrial flux.

~~Flask samplings of CO_2~~Atmospheric samples near the surface ~~concentrations with~~were collected at monthly intervals ~~are collected~~and analysed for CO_2 through the National Oceanic and Atmospheric Administration's (NOAA's) Earth System Research Laboratory (ESRL) at four sites (locations shown in Fig.1(~~a~~)) within our ~~modelling~~study domain, including Dongsha Island (DSI, 20.69˚N, 116.73˚E), Lulin (LLN, 23.47˚N, 120.87˚E), Ulaan Uul (UUM, 44.45˚N, 111.09˚E), and Mt. Waliguan (WLG, 36.29˚N, 100.89˚E). The Orbiting Carbon Observatory-2 (OCO-2) satellite product (Kiel et al., 2019) with daily intervals ~~is~~was employed to validate simulation of column averaged CO_2 (XCO_2) concentrations. A total of 204,940 OCO-2 version9 swath data covering the simulation period ~~is~~was used in this study. Daily ground-based Fourier transform spectrometer (FTS) Measured XCO_2 at Hefei site (31.90˚N, 117.17˚E) ~~is~~was also collected through the Total Carbon Column Observing Network (TCCON) for year 2016 (Wang et al., 2017). The TCCON-Hefei site was located in the northwestern rural area of Hefei city and measurements were conducted from September 2015 to December 2016 (Liu, 2018). WRF has been evaluated extensively and consistently performs well for reproducing the meteorology fields and the transport of atmospheric tracers~~,~~ in China (Gao et al., 2015;Tang et al., 2016;Wang et al., 2017;Yang et al., 2019), so this study will only present the simulation performance for CO_2 ~~only~~ which hasn't been thoroughly discussed in the literature.

3 Result and Discussion

3.1 Model evaluation

We first evaluate the capability of WRF-VPRM to reproduce concentrations of surface CO_2 and XCO_2, and we find fairly good model performance through the comparison with satellite and ground-based observations. The WRF-VPRM simulated surface layer (mid-level height AGL is 12m) CO_2 and XCO_2 averages between 2016-2018 are demonstrated in Fig.~~2~~3(a) and (b) respectively. High concentrations ~~are~~were found over industrial areas such as the North China Plain (NCP), Pearl River Delta (PRD), and Yangtze River Delta (YRD), where the surface CO_2 and XCO_2 ~~are~~were above 440 ppmv and 408 ppmv, respectively; the domain averages ~~are~~were 411 ppmv and 406 ppmv, respectively. While most climate models assume evenly distributed CO_2 (Fung et al., 1983;Kiehl and Ramanathan, 1983), our data demonstrates a prominent gradient between industrial and remote areas (e.g., Tibet Plateau, Mongolia), especially for surface CO_2, which could be an important source of uncertainty for estimating the long-wave radiation effect (Xie et al., 2018). Spatial patterns of CO_2 and XCO_2 ~~are~~were in close agreement with ODIAC, indicating the dominant impact of anthropogenic emission in determining the CO_2 distribution. WRF-VPRM simulated CO_2 ~~is~~was generally consistent with CT2019 (Fig.~~2(d~~3(c)), but CT2019 ~~estimates lower~~estimated near surface CO_2 (mid-level height AGL is 25m) over the coastal industrial areas YRD and PRD because the ocean module used in CT2019 ~~estimates~~estimated stronger air-sea exchange than the ocean flux by Takahashi et al. (2009) used in WRF-VPRM. The two models ~~show~~showed better agreement for XCO_2 (Fig.~~2~~3 (b) and (e)), but also ~~differ~~differed by ~1 ppmv over Taklamakan Desert and along the eastern side of the Tibet Plateau. The OCO-2 swath data ~~are~~were integrated into the corresponding horizontal grids of WRF-VPRM and CT2019~~,~~ respectively, to validate XCO_2. Biases of WRF-VPRM and CT2019 both fall into the range of $\pm$3 ppmv as shown in Fig.~~2(d~~3(c) and (f), respectively, but WRF-VPRM apparently ~~provides~~provided more details of spatial gradient. WRF-VPRM ~~shows~~showed well-mixed underestimations and overestimations along neighbouring satellite tracks, while CT2019 ~~tends~~tended to overestimate (underestimate) over Tibet Plateau (Taklamakan Desert) where WRF-VPRM ~~gives~~gave slightly smaller biases. Fig.4(a) and (b) present the raw data pairs between models and OCO-2 with daily interval for WRF-VPRM and CT2019, respectively. In general, the WRF-VPRM model ~~reproduces~~reproduced OCO-2 well, with mean bias (MB) of 0.76 ppmv, and ~~normalized mean bias (NMB) of 0.19% (Fig.3(a));~~ CT2019 ~~shows~~showed MB of 0.54 ppmv ~~and NMB of 0.17% (Fig.3(b)),~~ suggesting an overall acceptable performance of the weather-biosphere model to ~~reproduce~~simulate the spatial distribution pattern of XCO_2 in China.

We further analyse WRF-VPRM validation against OCO-2 for the seven vegetation types in each season and find no prominent difference (evaluation statistics summarized in Table 1). Regarding vegetation type, the model ~~shows~~showed the largest ~~normalized mean bias (NMB)~~ MB over deciduous forest of ~~-0.25%~~1.01 and ~~0.31%~~1.27 ppmv in summer and winter, respectively, ~~both over deciduous forest~~ which only ~~covers~~covered a very small portion in northeast China ~~(see dominant vegetation types in Fig.1(c)).~~ The three most abundant coverage vegetation types in China are grass, crops, and mixed forest. XCO_2 simulated by WRF-VPRM over grass areas ~~is~~was slightly overestimated by 0.~~08~~31~0.~~16%~~68 ppmv throughout the year, and the ~~NMB~~MB over mixed forest ~~is~~was -0.~~11%~~43~0.~~15%~~59 ppmv, indicating a good performance of the model over the

vast majority of areas of China. Performance over crops generally ~~shows~~showed larger discrepancy than other vegetation types, with ~~NMB~~MB ranging from 0.~~16%~~66 ppmv in summer to ~~0.29%~~1.19 ppmv in winter, suggesting the model tends to slightly overestimate column concentration of CO_2 over cropland. Li et al. (2020) reported that WRF-VPRM underestimated biosphere carbon over rice paddy sites (by ~3%) in northeast China and suggested the parameterization of α, β, λ as the most important cause. Cropland differs significantly across China with various types of species such as rice, wheat, and corn, for which ~~literature reports~~literatures reported substantially different rates of ecosystem respiration and photolysis uptake (Gao et al., 2018;Yang et al., 2016;Zhu et al., 2020). Thus, applying one set of parameters to represent all crops may be responsible for the lingering uncertainty of simulated XCO_2. In terms of seasonal difference, WRF-VRPM ~~performs best~~showed slightly smaller bias in summer ~~(NMB=0.12%)~~ and ~~worst~~larger bias in winter ~~(NMB=0.23%),~~ and the correlation coefficients ~~are~~were all ~0.8, consistent with application over the U.S. (Hu et al., 2020) which also reported slightly better performance in summer than other seasons~~, indicating good agreement with the OCO-2 satellite product~~.

Fig.~~3~~4 also presents the overall simulation bias against ground-based observations ~~employed in this study~~ at ~~the~~their raw temporal intervals (~~daily~~monthly for ~~OCO-2, daily for TCCON~~data at ~~Hefei~~ESRL sites, hourly for tower data at Lin'an, and ~~monthly~~daily for ~~data~~TCCON at Hefei). At the ESRL sites~~). Surface~~ (Fig.4(c)), surface CO_2 concentrations ~~are~~were simulated well with minor overestimation by 0.69 ppmv ~~(0.17%) at the ESRL sites (Fig.3(f)). However, evaluation~~. Evaluation at the Lin'an station ~~shows significant overestimations for CO_2 by 5.34 ppmv (1.25%) and 5.41 ppmv (1.27%) at 21m (Fig.3(d)) and 55m (Fig.3(e)) AGL, respectively; the~~was performed with the 4km-grid simulation. The mid-level heights of WRF-VPRM's first, second, and third layers ~~are~~were 12.3m, 36.9m, and 61.6m, respectively, and simulations ~~are~~were linearly interpolated to 21m and 55m to compare with the tower data. The evaluation at 21m AGL (Fig.4(d)) shows slight overestimation by 0.02 ppmv, but the evaluation at 55m height (Fig.4(e)) shows relatively large overestimations by 1.06 ppmv. The discrepancy is ~~largely attributable~~likely due to the combined effect of vertical allocation of anthropogenic emission ~~within the model as recently recognized~~ (Brunner et al., 2019)~~. Biosphere~~ and parameterization of VPRM. Tracer transport models (such as WRF-VPRM and CASA) and inverse modelling methods allocate anthropogenic CO_2 emission into the near surface layer due to lack of injection height information, which ~~will likely~~may subsequently lead to systematic overestimation of surface CO_2 concentration in industrial areas~~; though~~. Through a regional scale (750×650km) modelling study around the city of Berlin ~~(~~, Brunner et al.~~,~~. (2019) reported that distributing anthropogenic emission into the surface layer overestimated near-surface CO_2 concentration by 14% in summer and 43% in winter as compared with considering the vertical profiles of local anthropogenic sources. Lin'an observation tower is located at a densely vegetated area. Validation against OCO-2 suggested that WRF-VPRM did not show significantly different performance over different vegetation types as shown in Table 1. As compared to the ESRL background sites which were located in more remote areas with little anthropogenic emission (Fig.1(a)), Lin'an was more frequently affected by regional anthropogenic emissions which were transported from Shanghai and Hangzhou due to the prevailing northeast wind (Pu et al., 2014), indicating that the emission allocation discrepancy may induce more prominent error at Lin'an. In fact, the 20km-grid WRF-VPRM simulation bias at Lin'an were 5.34 and 5.41 ppmv at 21m and at 55m

respectively (Figure S2), significantly larger than the bias at ESRL sites. In addition, both the 20km-grid and 4km-grid simulations showed relatively larger bias at 55m than 21m due to smaller topography roughness and higher wind speed which increases with height according to observations (Figure S3). CT2019 also substantially ~~overestimates~~overestimated at Lin'an, but the first, second, and third layers' mid-level heights are 25m, 103m, and 247m, respectively, so we ~~did~~do not ~~compare it directly~~present the direct comparison with the tower data~~, but analysed the simulated diurnal variation as will be discussed in Section 3.3. Fig.3(c) and (d) reveal that observed average CO_2 concentrations at Lin'an (428 ppmv) are substantially higher than those at ESRL sites (407-410 ppmv). The evaluation at Lin'an station also infers the prominent high CO_2 level in YRD due to the intensive regional anthropogenic emission as compared with ESRL sites at remote locations. Pu et al. (Pu et al., 2014) analysed the back trajectories for hourly measurements collected at Lin'an station between 2009-2011 and demonstrated that it was frequently affected by prevailing northeast winds carrying polluted airmasses from upwind cities including Hangzhou, Shanghai, and northeast parts of Jiangsu where manufacturing factories were densely located.~~. Simulated XCO_2 ~~is also compared with~~ from both WRF-VPRM and CT2019 were well consistent with the TCCON Hefei site observations~~, and a very good agreement is found~~ as shown in Fig.4(f), with MB ~~of~~by -0.79 ppmv and ~~NMB of -0.2%. In general, recent~~ 0.78 ppmv respectively, and NMB by -0.20% and -0.19% respectively. The 4km-grid simulation showed very similar result to the 20-grid simulation for XCO_2 (Figure S1 and Figure S2). Recent atmospheric inverse modelling studies (Fu et al., 2019a;Wang et al., 2019;Xie et al., 2018) ~~report~~reported the simulation bias of XCO_2 as 0.5-2 ppmv with posterior flux inputs. The WRF-VPRM model applied in this study has demonstrated good agreement with the observations ~~as a process-based model~~ though our evaluation.

3.2 CO_2 seasonal variation and trend in China

We next analyse the seasonality of CO_2 and XCO_2 and find that the terrestrial flux ~~plays~~played a more influential role than anthropogenic emission. WRF-VPRM successfully ~~reproduces~~reproduced seasonal variations of CO_2 at ESRL sites, with a correlation coefficient of 0.90 (Fig.45(a~~)), but the~~)). The WRF-VPRM 4km-grid simulation showed a correlation ~~between simulated and observed CO_2 at~~ coefficient of 0.82 with the Lin'an tower ~~is only 0.67 (Fig.4(c)); we will probe into bias at Lin'an in the next section.~~observation (averaged for daytime 21m and 55m data). Both the model and measurements ~~show~~showed prominent seasonal cycles for surface CO_2 concentrations~~, with maximums~~. The WRF-VPRM simulation showed maxima in April (413-419 ppmv) and ~~minimums~~minima in August (399-404 ppmv) as ~~shown~~presented in Fig.45(b). The model ~~suggests~~suggested that the anthropogenic CO_2 contribution ~~is~~was 2.6 ppmv in both months, while the biogenic contributions ~~are~~were 3.1~~ ppmv~~ and -1.2 ppmv in April and August, respectively (Fig.45(d)). Anthropogenic emission (Fig.45(f)) ~~shows~~showed a flat curve with relatively higher values in December due to fuel combustion for heating (Zheng et al., 2018)~~;~~. EVI ~~meanwhile shows maximums~~showed maxima in July and August (Fig.45(f)). During summer, photosynthetic uptake almost completely ~~offsets~~compensated anthropogenic emission, causing the minimum CO_2 concentration observed in August, while the higher anthropogenic emission in December and respiration flux in April ~~lead~~led to the two corresponding peaks. The anthropogenic XCO_2 contributions ~~from are~~were 0.5 and 0.6 ppmv in April and August, respectively, and the

biogenic contributions ~~are~~were 0.8 ~~ppmv~~ and -1.5 ppmv, respectively, suggesting that the seasonality of XCO_2 ~~is~~was also primarily dominated by terrestrial flux. Furthermore, the seasonality at high-latitude ESRL sites (UUM and WLG) ~~is~~was stronger than at Lin'an and low-latitude sites (DSI and LLN) because of the larger temperature and photosynthetically active radiation (PAR) gradients. Annual average anthropogenic and biogenic XCO_2 contributions ~~are~~were 7.1 ~~ppmv~~ and -1.9 ppmv, respectively, indicating that biosphere uptake ~~is~~was an important carbon sink offsetting 27% of anthropogenic emission and slowing the growth of atmospheric CO_2.

XCO_2 ~~shows~~showed similar seasonality, with ~~minimums~~minima in August and ~~maximums~~maxima in April and December (Fig.~~4~~5(b)). Both WRF-VPRM and CT2019 ~~show~~showed good agreement with TCCON Hefei observations with correlations of 0.89 and 0.88, respectively (Fig.~~4~~5(e)). However, we note that WRF-VPRM ~~simulates~~simulated drastic changes (e.g., the grey shaded period in Fig.~~4~~5(e)) that ~~are~~were not ~~shown~~reproduced by CT2019~~;~~. Fig. ~~5~~6 shows the daily concentrations of XCO_2 overlaid with horizontal wind speed at 10m AGL from WRF-VPRM and CT2019 and highlights large discrepancies over Hefei. (Figure S4 shows the same comparison but using WRF-VPRM 4km-grid simulation data). Between April 1st and 3rd 2016, an 850 hPa trough associated with a surface cold front moved southeastward from Mongolia to the North China Plain (NCP) (weather maps shown in Fig.~~5~~6(g)-(i)). At the leading edge of the front, a convergence zone associated with a low pressure center formed, which led to significant cloud formation and subsequently reduced short-wave radiation. As a result, photosynthetic carbon uptake was reduced, leading to enhancement of atmospheric CO_2. Meanwhile, the cold front transported anthropogenic CO_2 from NCP to YRD, and the convergence zone along YRD ahead of the front facilitated the accumulation of air pollutants and CO_2 from anthropogenic emissions. With its coarse spatiotemporal resolution, CT2019 ~~has~~had difficulty reproducing such regional weather systems that can lead to rapid and localized changes in CO_2 concentration and terrestrial flux, indicating the importance of fine resolution modelling to better represent the small spatial scale and rapid temporal scale variations of CO_2 (Agusti-Panareda et al., 2019).

We also find a notable increasing trend for the 3-year study period. Observed CO_2 annual enhancement ~~is 0.56%/yr (~~was 2.2 ppmv/yr (0.56%/yr) at the ESRL sites and 2.3 ppmv/yr (0.~~67%/yr (2.8 ppmv/~~54%/yr) at Lin'an. The observed average CO_2 concentrations at Lin'an (428 ppmv) were substantially higher than those at ESRL sites (407-410 ppmv). The prominent higher levels of CO_2 and slightly higher absolute growth rate at Lin'an can be attributed to the influence of the transport regional anthropogenic emission~~,~~ which is growing at rate of 0.82%/yr as suggested by ODIAC. Domain-wide XCO_2 ~~is~~was also found to increase by ~~0.57%/yr (~~2.3 ppmv/yr (0.57%/yr) as suggested by OCO-2 and ~~0.61%/yr (~~2.5 ppmv/yr (0.61%/yr) as suggested by the simulation. WRF-VPRM ~~reproduces~~reproduced the trends in good agreement with ground and satellite observations. Model simulated budgets ~~suggests~~suggested that the increasing trends for anthropogenic, biogenic, and background XCO_2 ~~are~~were 0.81%/yr, -9.17%/yr, and 0.59%/yr, respectively; the trends for anthropogenic, biogenic, and background CO_2 ~~are~~were 4.95%/yr, -0.73%/yr, and 0.59%/yr, respectively. Our findings are consistent with recent measurements and inverse modelling studies but provide process-based estimates for anthropogenic emission and terrestrial flux. Wu et al. (Wu et al., 2012) reported measured CO_2 concentration at Changbai Mountain forest site in northeast China increased by 1.76 ppmv/yr between 2003-

2010. With the atmospheric inversion modelling method, Fu et al. (2019b) estimated surface CO_2 in East Asia increased by 2-3 ppmv/yr between 2004-2012. These trends suggest that although anthropogenic emission ~~increased~~increases at a steady rate in East Asia, photosynthetic uptake also ~~served~~serves as an increasing carbon sink due to enhanced EVI (0.29%/yr). However, as the interannual variability (IAV) of terrestrial flux is usually critically large and is affected by both vegetation itself and climate conditions (Fu et al., 2019b;Niu et al., 2017), simulation over longer time periods is necessary in future studies to conclusively comment on the changing trend of biosphere CO_2 in China.

3.3 Diurnal variation of near-surface CO_2 and influence factors

Finally, we examine the diurnal variation of ~~meteorology and~~ CO_2 data at Lin'an station as shown in Fig.~~6~~7 to reveal the temporal dynamics and atmospheric mixing of CO_2 at local scale. While both 21m (Fig.7(a)) and 55m (Fig.7(b)) CO_2 show prominent diurnal changes, the variations ~~are~~were larger in summer (JJA) than winter (DJF) and ~~are~~were larger at 21m than 55m, indicating the dominant influence of terrestrial flux over anthropogenic emission in determining the near surface CO_2 concentration. Fig.~~6~~7(c) ~~presents the diurnal change of wind speed collected at 50m of the Lin'an tower. The higher wind speed between 10:00-22:00 local time suggests strong regional transport~~ and ~~mixing of CO_2 mainly occurs during this period. Fig.6~~(d) ~~and (g)~~ present the WRF-VPRM ~~and CT2019~~ simulation bias~~,~~ at 21m and 55m respectively, ~~against Lin'an tower data at 21m (note the Y-scales are different).~~and Fig.7(e) and (f) present the bias of CT2019 at 21m and 55m respectively. We find that both models prominently ~~overestimate during night time,~~overestimated during nighttime, which shall be attributed to the bias in simulating NEE. Li et al. (2020) reported the model overestimated nighttime NEE at a mixed forest site Wuying (47.15˚N, 131.94˚E) by 34% during the growing season (May-Sep.) according to ~~EC~~eddy-covariance tower measurement. Fig.~~6(f~~7(g) and (~~i~~h) present the simulated NEE by WRF-VPRM and CT2019, respectively, which show close correlations with the CO_2 simulation biases. While Lin'an is also covered by mixed forest, our evaluation suggests that WRF-VPRM may ~~have~~ also ~~estimated~~overestimate nighttime ecosystem respiration ~~during the non-growing season,~~at Lin'an as it has a warmer climate condition than Wuying (Figure S5), and CT2019 has even greater bias for presenting the diurnal cycles of terrestrial flux.

We also find that planetary boundary layer height (PBLH) significantly affects diurnal accumulation and depletion of atmospheric CO_2 as shown in Fig.~~7~~8(a). During daytime in the growing season, photosynthetic uptake results in lower CO_2 concentration; meanwhile, PBLH is also high and allows rapid vertical mixing between near surface and upper air. During nighttime when photosynthesis stops, CO_2 from ecosystem respiration starts to accumulate in the shallow stable boundary layer, while the residual layer remains largely decoupled. Thus, atmospheric constituents with surface sources normally exhibit a vertical profile in which concentrations decrease with height in the stable boundary layer (Hu et al., 2020;Hu et al., 2012). Such boundary layer characteristics are confirmed by CO_2 vertical gradients at Lin'an~~.~~ in this study. CO_2 at 55m height ~~is~~was consistently lower than the near surface air at 21m during nighttime due to accumulation of respired CO_2 in the stable boundary layer. As photosynthetic uptake ~~depletes~~depleted the near surface CO_2 and daytime boundary layer convection ~~develops~~developed, the CO_2 gradient ~~is~~was gradually weakened from 06:00 to 11:00 LT and ~~remains~~remained minimal through

the rest of the daytime; at midday when photosynthesis reaches maximum intensity, CO_2 at 21m ~~is~~was even lower than at 55m. WRF-VPRM ~~generally reproduces~~roughly reproduced the diurnal profile but noticeably ~~underestimates~~underestimated the intensity of ~~night time~~ nighttime CO_2 difference (ΔCO_2~~,~~) likely due to the bias for simulating night time terrestrial flux as discussed above or underestimation of nighttime boundary layer stability by the PBL scheme (Hu et al., 2012).

The relationship between the near-surface CO_2 profile and boundary layer stability is further statistically examined. Fig.~~7~~8(b) presents the correlation between air temperature gradient ($\Delta T/\Delta H$) and CO_2 concentration gradient ($\Delta CO_2/\Delta H$) calculated with ~~annual averaged~~ diurnal profiles of tower observations~~, which~~ averaged for 2016-2018, where ΔT, ΔH, and ΔCO_2 is the differences of temperature, height, and CO_2 concentration between the two tower levels, respectively. Fig.8(b) clearly demonstrates the influence of boundary layer stability on the CO_2 vertical profile, as the correlation between $\Delta T/\Delta H$ and $\Delta CO_2/\Delta H$ reaches -0.98. On one hand, a more stable PBL with a strongly positive temperature gradient would promote surface CO_2 accumulation and lead to a strongly negative CO_2 gradient, especially under inversion conditions when upper air has higher temperature (orange area in Fig.~~7~~8(b)). Conversely, a strongly negative temperature gradient indicates stronger radiation, and subsequently greater photosynthesis and CO_2 depletion in the near surface layer, which would result in a positive CO_2 gradient (green area in Fig.~~7~~8(b)) implying a lower CO_2 concentration at the surface. While the diurnal variations of ΔCO_2 ~~are~~were primarily dictated by local biogenic CO_2 fluxes and boundary layer dynamics, the two minor daytime peaks of ΔCO_2 at Lin'an, at 10:00 and 18:00 LT (Fig.~~7~~8(a)) likely suggest influence of transport of CO_2 from urban plumes in the region; for example, from Hangzhou which is 60 km away from the tower. Due to rush-hours anthropogenic emissions, CO_2 enhancement at Hangzhou relative to a background site ~~exhibits~~exhibited a prominent bimodal curve with two peaks during early morning and early evening (Pu et al., 2018). Depending on meteorological conditions, particularly wind fields, urban CO_2 plumes from cities such as Hangzhou may be transported to the Lin'an site. ~~Due to higher altitude and stronger winds – wind profile increases with height at Lin'an according to observations (Figure S4) – 55m at the Lin'an tower has a larger footprint than 21m, thus 55m on the tower is more likely affected by the urban plumes in the region than 21m. The 10:00 and 18:00 LT ΔCO_2 peaks at Lin'an likely suggest stronger CO_2 enhancement at 55m than at 21m from influence of regional anthropogenic emissions; the slight delay of these ΔCO_2 peaks relative to rush hours (at about 08:00 and 17:00 LT) further corroborate the hypothesis of delayed influence of transport of urban CO_2 from Hangzhou. Even though 55m has a larger footprint than at 21m and thus may be more likely affected by regional urban emissions, turbulent vertical mixing may reduce the different influence from regional urban emissions, which explains the fact that ΔCO_2 peaks are only minor.~~ The influence of boundary layer conditions on CO_2 variability has been discussed in several studies through analysis of mountain site ground-based observations (Arrillaga et al., 2019;Esteki et al., 2017;Li et al., 2014), but our study ~~applies~~applied tower data as direct evidence to demonstrate the significant impact of PBL thermal structure, which has rarely been documented. More importantly, although WRF-VPRM ~~fails~~failed to capture the bimodal ΔCO_2 peaks at rush hours, because monthly ODIAC data ~~lacks~~lacked an hourly profile, our analysis reveals the critical importance of careful configuration of the PBL scheme and spatiotemporal distribution of anthropogenic emission for weather-biosphere modelling of atmospheric CO_2.

4 Summary and Conclusions

In this study, the spatiotemporal variations of CO_2 in China are investigated with measurements from multiple datasets and a weather-biosphere coupled model simulation for 2016-2018. We find consistent higher concentrations over industrial areas with excessive anthropogenic emission and lower concentrations over densely vegetated areas. Observed CO_2 concentrations at Lin'an (427 ppmv) are significantly higher than remote ESRL sites (408 ppmv) although they are all established as "background" stations, indicating the dominant influence of anthropogenic emission at regional scales. The Lin'an tower data shows a large negative correlation (-0.8598) between vertical CO_2 concentration and air temperature gradients, suggesting the significant influence of boundary layer stability on CO_2 accumulation and depletion. The online coupled weather-biosphere model WRF-VPRM enables process-based estimations of contributions from anthropogenic emission (0.59 ppmv (0.15%)), terrestrial flux (0.16 ppmv (-0.04%)), and background concentration (405.70 ppmv (99.89%)) –to average total XCO_2. Respective simulation biases of surface CO_2 and XCO_2 are 0.69 ppmv (0.17%) and 0.76 ppmv (0.19) against ESRL site observations and OCO-2 satellite product with correlations of 0.87 and 0.90, indicating overall good performance of the WRV-VPRM model. Maximum CO_2 concentrations are found in April and minimumsminima are found in August for all three years, and the seasonality is reproduced well by the model, which also reveals that terrestrial flux and background concentration dominated the seasonality rather than anthropogenic emission.

A steadily increasing trend in XCO_2 by ~2.46 ppmv (~0.6%/yr) during the study period is demonstrated consistently by both model simulation and satellite product. Budget analysis suggests that anthropogenic emission increased by 0.83%/yr contributing to the 0.81%/yr growth rate of anthropogenic XCO_2 enhancement, 27% of which was offset by biosphere uptake. It is noted that terrestrial flux has significant inter-annual variability, thus a more robust estimation of the terrestrial flux trend should be obtained through a long-term study in the future. The background XCO_2, representing contributions from global circulation, increased by 2.37 ppm (0.59%/yr,), suggesting that CO_2 level in China was growing at the same rate as the rest of the world.

The most significant modelling bias is identified from validation against the Lin'an tower data55m observations, which WRF-VPRM 4km-grid simulation overestimated by about 5.381.06 ppmv (1.26%) with a correlation coefficient of 0.6782. The allocation of anthropogenic emission into the surface layer is partially responsible for this modelling bias because Lin'an is closely affected by upwind industrial mega cities in YRD, suggesting the need to include vertical profiles of fossil fuel combustion to properly redistribute the ODIAC for modelling purposes. HoweverIn addition, diurnal variations of the bias suggest that the modelling discrepancy is likely due toalso induced by large uncertainty associated with simulating nighttime ecosystem respiration during the nighttime. Representation and parameterization of photosynthetic carbon uptake in VPRM has been continuously improved during the past 10 years since its first release (Hu et al., 2020), but ecosystem respiration parameterization is still too simplified to fully represent the autotrophic and heterotrophic respiration of biomass. Li et al. (2020) and our study both reveal the urgent need to better calibrate VPRM parameterization over different vegetation types in China, and other methods such as inverse modelling is necessary to further validate the anthropogenic fluxes from ODIAC.

Nevertheless, WRF-VPRM is demonstrated to be a reliable tool to model the dynamics of CO_2 and exchange between the atmosphere and terrestrial flux. Most importantly, as the online coupled modelling system is able to simulate meteorology and biosphere processes simultaneously, it promotes the opportunity to investigate the interactions between atmospheric mixing and terrestrial flux (Carvalhais et al., 2014;Schimel et al., 2015) while comprehensively considering various factors from both sides that affect CO_2 in one coordinate frame, which could be a very helpful tool to support policy makers for balancing short-term carbon cycles at regional scales.

Data availability

The modelling output is accessible by contacting the corresponding author (yjjiang@pku.org.cn, xhu@ou.edu)

Author contributions

The concept and ideas to design the integrated simulation and observation analysis ~~were~~are devised by YJ, X-MH, and XD. Simulation ~~was~~is performed by X-MH. OCO-2 satellite product ~~was~~is collected and processed by X-MH. CT2019 assimilation data and ground-based observations ~~were~~are collected by XD. Tower measurement ~~was~~is conducted, processed, and analysed by QM, JP, and YJ. Model evaluation ~~was~~is performed by MY. The manuscript ~~was~~is prepared by XD and X-MH with input and feedback from YJ, MY, QM, JP, and GZ.

Competing interests

The authors declare that they have no conflict of interest.

Acknowledgements

This work is supported by the Fundamental Research Funds for the Central Universities (14380049) and National Key Research and Development Program of China (2016YFC0201900). We thank NASA and NOAA ESRL for providing the public accessible satellite products and observations used in this study. OCO-2 data was collected through https://co2.jpl.nasa.gov/#mission=OCO-2. ESRL surface flask CO_2 data was downloaded from https://www.esrl.noaa.gov/gmd/dv/data.html. TCCON data was downloaded from https://data.caltech.edu/records/1092. ~~CarbonTracker~~CT2019B results were provided by NOAA ESRL, Boulder, Colorado, USA from the website at http://carbontracker.noaa.gov~~CarbonTracker~~ data was downloaded from https://www.esrl.noaa.gov/gmd/ccgg/carbontracker/download.php.

References

Agusti-Panareda, A., Diamantakis, M., Massart, S., Chevallier, F., Munoz-Sabater, J., Barre, J., Curcoll, R., Engelen, R., Langerock, B., Law, R. M., Loh, Z., Morgui, J. A., Parrington, M., Pench, V. H., Ramonet, M., Roehl, C., Vermeulen, A. T., Warneke, T., and Wunch, D.: Modelling CO2 weather - why horizontal resolution matters, Atmos Chem Phys, 19, 7347-7376, 2019.

Ahmadov, R., Gerbig, C., Kretschmer, R., Koerner, S., Neininger, B., Dolman, A. J., and Sarrat, C.: Mesoscale covariance of transport and CO2 fluxes: Evidence from observations and simulations using the WRF-VPRM coupled atmosphere-biosphere model, J Geophys Res-Atmos, 112, 2007.

Ahmadov, R., Gerbig, C., Kretschmer, R., Korner, S., Rodenbeck, C., Bousquet, P., and Ramonet, M.: Comparing high resolution WRF-VPRM simulations and two global CO2 transport models with coastal tower measurements of CO2, Biogeosciences, 6, 807-817, 2009.

Arrillaga, J. A., Yague, C., Roman-Cascon, C., Sastre, M., Jimenez, M. A., Maqueda, G., and de Arellano, J. V. G.: From weak to intense downslope winds: origin, interaction with boundary-layer turbulence and impact on CO2 variability, Atmos Chem Phys, 19, 4615-4635, 2019.

Brunner, D., Kuhlmann, G., Marshal, J., Clement, V., Fuhrer, O., Broquet, G., Loscher, A., and Meijer, Y.: Accounting for the vertical distribution of emissions in atmospheric CO2 simulations, Atmos Chem Phys, 19, 4541-4559, 2019.

Carvalhais, N., Forkel, M., Khomik, M., Bellarby, J., Jung, M., Migliavacca, M., Mu, M. Q., Saatchi, S., Santoro, M., Thurner, M., Weber, U., Ahrens, B., Beer, C., Cescatti, A., Randerson, J. T., and Reichstein, M.: Global covariation of carbon turnover times with climate in terrestrial ecosystems, Nature, 514, 213-+, 2014.

Chen, F., and Dudhia, J.: Coupling an advanced land surface-hydrology model with the Penn State-NCAR MM5 modeling system. Part I: Model implementation and sensitivity, Mon Weather Rev, 129, 569-585, 2001.

Crowell, S. M. R., Kawa, S. R., Browell, E. V., Hammerling, D. M., Moore, B., Schaefer, K., and Doney, S. C.: On the Ability of Space-Based Passive and Active Remote Sensing Observations of CO2 to Detect Flux Perturbations to the Carbon Cycle, J Geophys Res-Atmos, 123, 1460-1477, 2018.

Dayalu, A., Munger, J. W., Wofsy, S. C., Wang, Y. X., Nehrkorn, T., Zhao, Y., McElroy, M. B., Nielsen, C. P., and Luus, K.: Assessing biotic contributions to CO2 fluxes in northern China using the Vegetation, Photosynthesis and Respiration Model (VPRM-CHINA) and observations from 2005 to 2009, Biogeosciences, 15, 6713-6729, 2018.

Deng, J. J., Zhang, Y. R., Qiu, Y. Q., Zhang, H. L., Du, W. J., Xu, L. L., Hong, Y. W., Chen, Y. T., and Chen, J. S.: Source apportionment of PM2.5 at the Lin'an regional background site in China with three receptor models, Atmos Res, 202, 23-32, 2018.

Dudhia, J.: Numerical Study of Convection Observed during the Winter Monsoon Experiment Using a Mesoscale Two-Dimensional Model, J Atmos Sci, 46, 3077-3107, 1989.

Esteki, K., Prakash, N., Li, Y. L., Mu, C., and Du, K.: Seasonal Variation of CO2 Vertical Distribution in the Atmospheric Boundary Layer and Impact of Meteorological Parameters, Int J Environ Res, 11, 707-721, 2017.

Feng, S., Lauvaux, T., Keller, K., Davis, K. J., Rayner, P., Oda, T., and Gurney, K. R.: A Road Map for Improving the Treatment of Uncertainties in High-Resolution Regional Carbon Flux Inverse Estimates, Geophys Res Lett, 46, 13461-13469, 2019.

Fu, Y., Liao, H., Tian, X. J., Gao, H., Cai, Z. N., and Han, R.: Sensitivity of the simulated CO2 concentration to inter-annual variations of its sources and sinks over East Asia, Adv Clim Chang Res, 10, 250-263, 2019a.

Fu, Z., Stoy, P. C., Poulter, B., Gerken, T., Zhang, Z., Wakbulcho, G., and Niu, S. L.: Maximum carbon uptake rate dominates the interannual variability of global net ecosystem exchange, Global Change Biol, 25, 3381-3394, 2019b.

Fung, I., Prentice, K., Matthews, E., Lerner, J., and Russell, G.: 3-Dimensional Tracer Model Study of Atmospheric Co2 - Response to Seasonal Exchanges with the Terrestrial Biosphere, J Geophys Res-Oceans, 88, 1281-1294, 1983.

Gao, Y. H., Xu, J. W., and Chen, D. L.: Evaluation of WRF Mesoscale Climate Simulations over the Tibetan Plateau during 1979-2011, J Climate, 28, 2823-2841, 2015.

Gao, Y. Q., Lee, X. H., Liu, S. D., Hu, N., Hu, C., Liu, C., Zhang, Z., and Yang, Y. C.: Spatiotemporal variability of the near-surface CO2 concentration across an industrial-urban-rural transect, Nanjing, China, Sci Total Environ, 631-632, 1192-1200, 2018.

Gaubert, B., Stephens, B. B., Basu, S., Chevallier, F., Deng, F., Kort, E. A., Patra, P. K., Peters, W., Rodenbeck, C., Saeki, T., Schimel, D., Van der Laan-Luijkx, I., Wofsy, S., and Yin, Y.: Global atmospheric CO2 inverse models converging on neutral tropical land exchange, but disagreeing on fossil fuel and atmospheric growth rate, Biogeosciences, 16, 117-134, 2019.
Grell, G. A., and Devenyi, D.: A generalized approach to parameterizing convection combining ensemble and data assimilation techniques, Geophys Res Lett, 29, 2002.
Han, P. F., Zeng, N., Yao, B., Zhou, W. J., Chen, L. Q., Wang, S. Q., Lv, H. G., Xiao, W., Zhu, L. Y., and Xu, J. P.: Preface to Special Topic on Atmospheric Greenhouse Gas Measurement and Application in China, Adv Atmos Sci, 37, 555-556, 2020.
Hong, S. Y., Noh, Y., and Dudhia, J.: A new vertical diffusion package with an explicit treatment of entrainment processes, Mon Weather Rev, 134, 2318-2341, 2006.
Hu, X. M., Doughty, D. C., Sanchez, K. J., Joseph, E., and Fuentes, J. D.: Ozone variability in the atmospheric boundary layer in Maryland and its implications for vertical transport model, Atmos Environ, 46, 354-364, 2012.
Hu, X. M., Crowell, S., Wang, Q. Y., Zhang, Y., Davis, K. J., Xue, M., Xiao, X. M., Moore, B., Wu, X. C., Choi, Y., and DiGangi, J. P.: Dynamical Downscaling of CO2 in 2016 Over the Contiguous United States Using WRF-VPRM, a Weather-Biosphere-Online-Coupled Model, Jounal of Advances in Modeling Earth Systems, 12, 10.1029/2019MS001875, 2020.
Huang, X., Ding, A. J., Wang, Z. L., Ding, K., Gao, J., Chai, F. H., and Fu, C. B.: Amplified transboundary transport of haze by aerosol-boundary layer interaction in China, Nat Geosci, 13, 428-+, 2020.
Huete, A., Didan, K., Miura, T., Rodriguez, E. P., Gao, X., and Ferreira, L. G.: Overview of the radiometric and biophysical performance of the MODIS vegetation indices, Remote Sens Environ, 83, 195-213, 2002.
Jacobson, A. R., Schuldt, K. N., Miller, J. B., Oda, T., Tans, P., Andrews, A., Mund, J., Ott, L., Collatz,G. J., Aalto, T., Afshar, S., Aikin, K., Aoki, S., Apadula, F., Baier, B., Bergamaschi, P., Beyersdorf, A., Biraud, S. C., Bollenbacher, A., Bowling, D., Brailsford, G., Abshire, J. B., Chen, G., Chen, H., Chmura, L., Colomb, A., Conil, S., Cox, A., Cristofanelli, P., Cuevas, E., Curcoll, R., Sloop, C. D., Davis, K., Wekker, S. D., Delmotte, M., DiGangi, J. P., Dlugokencky, E., Ehleringer, J., Elkins, J. W., Emmenegger, L., Fischer, M. L., Forster, G., Frumau, A., Galkowski, M., Gatti, L. V., Gloor, E., Griffis, T., Hammer, S., Haszpra, L., Hatakka, J., Heliasz, M., Hensen, A., Hermanssen, O., Hintsa, E., Holst, J., Jaffe, D., Karion, A., Kawa, S. R., Keeling, R., Keronen, P., Kolari, P., Kominkova, K., Kort, E., Krummel, P., Kubistin, D., Labuschagne, C., Langenfelds, R., Laurent, O., Laurila, T., Lauvaux, T., Law, B., Lee, J., Lehner, I., Leuenberger, M., Levin, I., Levula, J., Lin, J., Lindauer, M., Loh, Z., Lopez, M., Luijkx, I. T., Lund Myhre, C., Machida, T., Mammarella, I., Manca, G., Manning, A., Marek, M. V., Marklund, P., Martin, M. Y., Matsueda, H., McKain, K., Meijer, H., Meinhardt, F., Miles, N., Miller, C. E., Molder, M., Montzka, S., Moore, F., Morgui, J.-A., Morimoto, S., Munger, B., Necki, J., Newman, S., Nichol, S., Niwa, Y., ODoherty, S., Ottosson-Lofvenius, M., Paplawsky, B., Peischl, J., Peltola, O., Pichon, J.-M., Piper, S., Plass-Dolmer, C., Ramonet, M., Reyes-Sanchez, E., Richardson, S., Riris, H., Ryerson, T., Saito, K., Sargent, M., Sasakawa, M., Sawa, Y., Say, D., Scheeren, B., Schmidt, M., Schmidt, A., Schumacher, M., Shepson, P., Shook, M., Stanley, K., Steinbacher, M., Stephens, B., Sweeney, C., Thoning, K., Torn, M., Turnbull, J., Tørseth, K., Bulk, P. V. D., Dinther, D. V., Vermeulen, A., Viner, B., Vitkova, G., Walker, S., Weyrauch, D., Wofsy, S., Worthy, D., Young, D., and Zimnoch, M.. : CarbonTracker CT2019B, DOI: 10.25925/20201008, 2020.
Kiehl, J. T., and Ramanathan, V.: Co2 Radiative Parameterization Used in Climate Models - Comparison with Narrow-Band Models and with Laboratory Data, J Geophys Res-Oceans, 88, 5191-5202, 1983.
Kiel, M., O'Dell, C. W., Fisher, B., Eldering, A., Nassar, R., MacDonald, C. G., and Wennberg, P. O.: How bias correction goes wrong: measurement of X-CO2 affected by erroneous surface pressure estimates, Atmos Meas Tech, 12, 2241-2259, 2019.
Kondo, M., Patra, P. K., Sitch, S., Friedlingstein, P., Poulter, B., Chevallier, F., Ciais, P., Canadell, J. G., Bastos, A., Lauerwald, R., Calle, L., Ichii, K., Anthoni, P., Arneth, A., Haverd, V., Jain, A. K., Kato, E., Kautz, M., Law, R. M., Lienert, S., Lombardozzi, D., Maki, T., Nakamura, T., Peylin, P., Rodenbeck, C., Zhuravlev, R., Saeki, T., Tian, H. Q., Zhu, D., and Ziehn, T.: State of the science in reconciling top-down and bottom-up approaches for terrestrial CO2 budget, Global Change Biol, 26, 1068-1084, 2020.
Kountouris, P., Gerbig, C., Rodenbeck, C., Karstens, U., Koch, T. F., and Heimann, M.: Atmospheric CO2 inversions on the mesoscale using data-driven prior uncertainties: quantification of the European terrestrial CO2 fluxes, Atmos Chem Phys, 18, 3047-3064, 2018.
Kretschmer, R., Gerbig, C., Karstens, U., and Koch, F. T.: Error characterization of CO2 vertical mixing in the atmospheric transport model WRF-VPRM, Atmos Chem Phys, 12, 2441-2458, 2012.

Li, X. L., Hu, X. M., Cai, C. J., Jia, Q. Y., Zhang, Y., Liu, J. M., Xue, M., Xu, J. M., Wen, R. H., and Crowell, S. M. R.: Terrestrial CO2 Fluxes, Concentrations, Sources and Budget in Northeast China: Observational and Modeling Studies, J Geophys Res-Atmos, 125, 2020.
Li, Y., Deng, J., Mu, C., Xing, Z., and Du, K.: Vertical distribution of CO2 in the atmospheric boundary layer: Characteristics and impact of meteorological variables, Atmos Environ, 91, 110-117, 2014.
Liu, C., Wang, W., Sun, Y.: TCCON data from Hefei, China, Release GGG2014R0. TCCON data archive, hosted by CaltechDATA, California Institute of Technology, Pasadena, CA, U.S.A., http://dx.doi.org/10.14291/tccon.ggg2014.hefei01.R0, 2018.
Mahadevan, P., Wofsy, S. C., Matross, D. M., Xiao, X. M., Dunn, A. L., Lin, J. C., Gerbig, C., Munger, J. W., Chow, V. Y., and Gottlieb, E. W.: A satellite-based biosphere parameterization for net ecosystem CO2 exchange: Vegetation Photosynthesis and Respiration Model (VPRM), Global Biogeochem Cy, 22, 2008.
Mlawer, E. J., Taubman, S. J., Brown, P. D., Iacono, M. J., and Clough, S. A.: Radiative transfer for inhomogeneous atmospheres: RRTM, a validated correlated-k model for the longwave, J Geophys Res-Atmos, 102, 16663-16682, 1997.
Morrison, H., Thompson, G., and Tatarskii, V.: Impact of Cloud Microphysics on the Development of Trailing Stratiform Precipitation in a Simulated Squall Line: Comparison of One- and Two-Moment Schemes, Mon Weather Rev, 137, 991-1007, 2009.
Niu, S. L., Fu, Z., Luo, Y. Q., Stoy, P. C., Keenan, T. F., Poulter, B., Zhang, L. M., Piao, S. L., Zhou, X. H., Zheng, H., Han, J. Y., Wang, Q. F., and Yu, G. R.: Interannual variability of ecosystem carbon exchange: From observation to prediction, Global Ecol Biogeogr, 26, 1225-1237, 2017.
Oda, T., Maksyutov, S., and Andres, R. J.: The Open-source Data Inventory for Anthropogenic CO2, version 2016 (ODIAC2016): a global monthly fossil fuel CO2 gridded emissions data product for tracer transport simulations and surface flux inversions, Earth Syst Sci Data, 10, 87-107, 2018.
Papale, D., and Valentini, A.: A new assessment of European forests carbon exchanges by eddy fluxes and artificial neural network spatialization, Global Change Biol, 9, 525-535, 2003.
Park, C., Gerbig, C., Newman, S., Ahmadov, R., Feng, S., Gurney, K. R., Carmichael, G. R., Park, S. Y., Lee, H. W., Goulden, M., Stutz, J., Peischl, J., and Ryerson, T.: CO2 Transport, Variability, and Budget over the Southern California Air Basin Using the High-Resolution WRF-VPRM Model during the CalNex 2010 Campaign, J Appl Meteorol Clim, 57, 1337-1352, 2018.
Park, C., Park, S. Y., Gurney, K. R., Gerbig, C., DiGangi, J. P., Choi, Y., and Lee, H. W.: Numerical simulation of atmospheric CO2 concentration and flux over the Korean Peninsula using WRF-VPRM model during Korus-AQ 2016 campaign, Plos One, 15, 2020.
Peters, W., Jacobson, A. R., Sweeney, C., Andrews, A. E., Conway, T. J., Masarie, K., Miller, J. B., Bruhwiler, L. M. P., Petron, G., Hirsch, A. I., Worthy, D. E. J., van der Werf, G. R., Randerson, J. T., Wennberg, P. O., Krol, M. C., and Tans, P. P.: An atmospheric perspective on North American carbon dioxide exchange: CarbonTracker, P Natl Acad Sci USA, 104, 18925-18930, 10.1073/pnas.0708986104, 2007.
Peylin, P., Baker, D., Sarmiento, J., Ciais, P., and Bousquet, P.: Influence of transport uncertainty on annual mean and seasonal inversions of atmospheric CO2 data, J Geophys Res-Atmos, 107, 2002.
Peylin, P., Law, R. M., Gurney, K. R., Chevallier, F., Jacobson, A. R., Maki, T., Niwa, Y., Patra, P. K., Peters, W., Rayner, P. J., Rodenbeck, C., van der Laan-Luijkx, I. T., and Zhang, X.: Global atmospheric carbon budget: results from an ensemble of atmospheric CO2 inversions, Biogeosciences, 10, 6699-6720, 2013.
Pu, J. J., Xu, H. H., He, J., Fang, S. X., and Zhou, L. X.: Estimation of regional background concentration of CO2 at Lin'an Station in Yangtze River Delta, China, Atmos Environ, 94, 402-408, 2014.
Pu, J. J., Hu, H. H., Jiang, Y. J., Du, R. G., and Qi, B.: Characteristics of and factors affecting atmospheric CO2 concentration in Hangzhou, Environmental Science, 39, 10.13227/j.hjkx.201708258, 2018.
Pu, J. J., Xu, H. H., Yao, B., Yu, Y., Jiang, Y. J., Ma, Q. L., and Chen, L. Q.: Estimate of Hydrofluorocarbon Emissions for 2012-16 in the Yangtze River Delta, China (vol 37, pg 576, 2020), Adv Atmos Sci, 37, 925-925, 2020.
Schimel, D., Stephens, B. B., and Fisher, J. B.: Effect of increasing CO2 on the terrestrial carbon cycle, P Natl Acad Sci USA, 112, 436-441, 2015.
Shi, Z., Crowell, S., Luo, Y. Q., and Moore, B.: Model structures amplify uncertainty in predicted soil carbon responses to climate change, Nat Commun, 9, 2018.

Takahashi, T., Sutherland, S. C., Wanninkhof, R., Sweeney, C., Feely, R. A., Chipman, D. W., Hales, B., Friederich, G., Chavez, F., Sabine, C., Watson, A., Bakker, D. C. E., Schuster, U., Metzl, N., Yoshikawa-Inoue, H., Ishii, M., Midorikawa, T., Nojiri, Y., Kortzinger, A., Steinhoff, T., Hoppema, M., Olafsson, J., Arnarson, T. S., Tilbrook, B., Johannessen, T., Olsen, A., Bellerby, R., Wong, C. S., Delille, B., Bates, N. R., and de Baar, H. J. W.: Climatological mean and decadal change in surface ocean pCO(2), and net sea-air CO2 flux over the global oceans (vol 56, pg 554, 2009), Deep-Sea Res Pt I, 56, 2075-2076, 2009.

Tang, J. P., Niu, X. R., Wang, S. Y., Gao, H. X., Wang, X. Y., and Wu, J.: Statistical downscaling and dynamical downscaling of regional climate in China: Present climate evaluations and future climate projections, J Geophys Res-Atmos, 121, 2110-2129, 2016.

Tian, H. Q., Lu, C. Q., Yang, J., Banger, K., Huntzinger, D. N., Schwalm, C. R., Michalak, A. M., Cook, R., Ciais, P., Hayes, D., Huang, M. Y., Ito, A., Jain, A. K., Lei, H. M., Mao, J. F., Pan, S. F., Post, W. M., Peng, S. S., Poulter, B., Ren, W., Ricciuto, D., Schaefer, K., Shi, X. Y., Tao, B., Wang, W. L., Wei, Y. X., Yang, Q. C., Zhang, B. W., and Zeng, N.: Global patterns and controls of soil organic carbon dynamics as simulated by multiple terrestrial biosphere models: Current status and future directions, Global Biogeochem Cy, 29, 775-792, 2015.

Todd-Brown, K. E. O., Randerson, J. T., Post, W. M., Hoffman, F. M., Tarnocai, C., Schuur, E. A. G., and Allison, S. D.: Causes of variation in soil carbon simulations from CMIP5 Earth system models and comparison with observations, Biogeosciences, 10, 1717-1736, 2013.

Wang, H. M., Jiang, F., Wang, J., Ju, W. M., and Chen, J. M.: Terrestrial ecosystem carbon flux estimated using GOSAT and OCO-2 XCO2 retrievals, Atmos Chem Phys, 19, 12067-12082, 2019.

Wang, W., Tian, Y., Liu, C., Sun, Y. W., Liu, W. Q., Xie, P. H., Liu, J. G., Xu, J., Morino, I., Velazco, V. A., Griffith, D. T., Notholt, J., and Warneke, T.: Investigating the performance of a greenhouse gas observatory in Hefei, China, Atmos Meas Tech, 10, 2627-2643, 2017.

Wu, J. B., Guan, D. X., Yuan, F. H., Yang, H., Wang, A. Z., and Jin, C. J.: Evolution of atmospheric carbon dioxide concentration at different temporal scales recorded in a tall forest, Atmos Environ, 61, 9-14, 2012.

Xie, X. D., Huang, X. X., Wang, T. J., Li, M. M., Li, S., and Chen, P. L.: Simulation of Non-Homogeneous CO2 and Its Impact on Regional Temperature in East Asia, J Meteorol Res-Prc, 32, 456-468, 2018.

Yang, S. H., Xu, J. Z., Liu, X. Y., Zhang, J. G., and Wang, Y. J.: Variations of carbon dioxide exchange in paddy field ecosystem under water-saving irrigation in Southeast China, Agr Water Manage, 166, 42-52, 2016.

Yang, Y., Hu, X. M., Gao, S. H., and Wang, Y. M.: Sensitivity of WRF simulations with the YSU PBL scheme to the lowest model level height for a sea fog event over the Yellow Sea, Atmos Res, 215, 253-267, 2019.

Zheng, B., Tong, D., Li, M., Liu, F., Hong, C. P., Geng, G. N., Li, H. Y., Li, X., Peng, L. Q., Qi, J., Yan, L., Zhang, Y. X., Zhao, H. Y., Zheng, Y. X., He, K. B., and Zhang, Q.: Trends in China's anthropogenic emissions since 2010 as the consequence of clean air actions, Atmos Chem Phys, 18, 14095-14111, 2018.

Zhou, Y., Williams, C. A., Lauvaux, T., Davis, K. J., Feng, S., Baker, I., Denning, S., and Wei, Y.: A Multiyear Gridded Data Ensemble of Surface Biogenic Carbon Fluxes for North America: Evaluation and Analysis of Results, Journal of Geophysical Research: Biogeosciences, 125, e2019JG005314, 10.1029/2019jg005314, 2020.

Zhu, Z. L., Tang, X. Z., and Zhao, F. H.: Comparison of Ozone Fluxes over a Maize Field Measured with Gradient Methods and the Eddy Covariance Technique, Adv Atmos Sci, 37, 586-596, 2020.

Table 1. Evaluation statistics[1] for WRF-VPRM 20km-grid simulation against OCO-2 satellite product at daily intervals

Season	Vegetation type	Mean Obs. (ppmv)	Mean Sim. (ppmv)	~~MB[2]~~ MB[1] (ppmv)	~~NMB[2]~~ (%)cc[1]	~~cc[2]~~	# of samples
Spring	other	406.85	407.81	0.9696[2]	~~0.23[1]~~	0.82	16123
	evergreen	407.52	407.89	0.36	~~0.09~~	0.73	1920
	deciduous	408.15	408.430	**0.27**	~~**0.07**[1]~~	0.82	412
	mixed	407.79	408.21	0.41	~~0.10~~	0.79	4438
	shrubland	406.97	407.54	0.56	~~0.13~~	0.74	6550
	savanna	407.59	408.55	0.96	~~0.22~~	0.81	534
	grass	406.81	407.49	0.68	~~0.16~~	0.81	11170
	crops	407.50	408.29	0.79	~~0.19~~	0.82	13548
Summer	other	403.90	404.84	0.93	~~0.23~~	0.88	13445
	evergreen	402.68	402.24	-0.44	~~-0.11~~	0.85	1082
	deciduous	400.39	399.39	-1.01	~~-0.25~~	0.82	527
	mixed	402.04	401.60	-0.43	~~-0.11~~	0.87	4312
	shrubland	403.92	404.41	0.48	~~0.12~~	0.85	5193
	savanna	404.62	404.60	**-0.02**	~~**0.01**~~	0.79	170
	grass	402.35	402.66	0.31	~~0.08~~	0.88	12588
	crops	402.86	403.52	0.66	~~0.16~~	0.87	7947
Fall	other	403.32	404.35	1.03	~~0.26~~	0.82	17054
	evergreen	403.93	403.19	-0.74	~~-0.18~~	0.71	1716
	deciduous	403.35	403.64	**0.28**	~~**0.07**~~	0.84	281
	mixed	403.64	403.95	0.31	~~0.08~~	0.83	3611
	shrubland	403.12	404.22	1.10	~~0.27~~	0.77	8532
	savanna	403.45	404.15	0.70	~~0.17~~	0.70	504
	grass	403.22	403.65	0.43	~~0.11~~	0.85	11176
	crops	403.76	404.80	1.04	~~0.26~~	0.80	13136
Winter	other	404.76	405.80	1.03	~~0.26~~	0.80	13838
	evergreen	404.79	404.75	**-0.05**	~~**-0.01**~~	0.78	2671
	deciduous	405.38	406.65	1.27	~~0.31~~	0.79	135
	mixed	405.20	405.79	0.59	~~0.15~~	0.79	2108
	shrubland	404.76	405.84	1.09	~~0.27~~	0.79	7683
	savanna	404.63	405.83	1.20	~~0.30~~	0.75	1064
	grass	405.06	405.64	0.58	~~0.14~~	0.77	5967
	crops	405.17	406.36	1.19	~~0.29~~	0.79	15508

~~[1]For each season, evaluation statistic with the worst performance (largest absolute value of NMB) is highlighted in red, and the one with best performance (smallest absolute value of NMB) is highlighted with in bold font.~~

~~[2] $MB = \frac{1}{N}\sum_{i=1}^{N}(Sim_i - Obs_i)$, $NMB = \frac{\sum_{i=1}^{N}(Sim_i - Obs_i)}{\sum_{i=1}^{N} Obs_i}$~~, [1] Mean bias was calculated as: $MB = \frac{1}{N}\sum_{i=1}^{N}(Sim_i - Obs_i)$, and correlation coefficient was calculated as: $cc = \frac{\sum_{i=1}^{N}(Sim_i - \bar{S}im)(Obs_i - \bar{O}bs)}{\sqrt{\sum_{i=1}^{N}(Sim_i - \bar{S}im)^2}\sqrt{\sum_{i=1}^{N}(Obs_i - \bar{O}bs)^2}}$, where $\bar{S}im$ is the average of simulations, $\bar{O}bs$ is the average of observations.

删除的单元格
带格式表格
删除的单元格
带格式的: 字体颜色: 红色
带格式的: 字体: 加粗
带格式的: 字体颜色: 红色
带格式的: 字体: 加粗
带格式的: 字体: 加粗
带格式的: 字体颜色: 红色
带格式的: 字体: 加粗
带格式的: 字体颜色: 红色
带格式的: 左
带格式的: 字体颜色: 文字 1, 上标

[2] For each season, evaluation statistic with the worst performance (largest absolute value of MB) is highlighted in red, and the one with best performance (smallest absolute value of MB) is highlighted with in bold font.

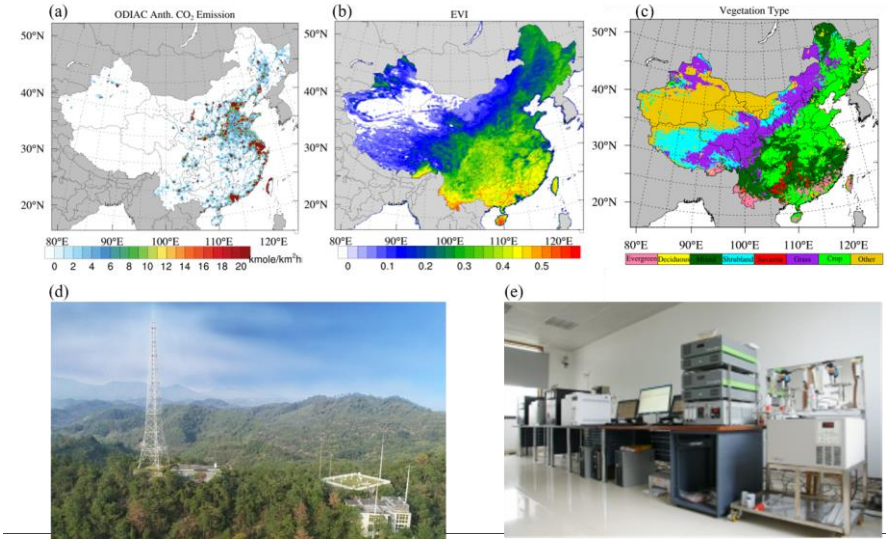
(a)
ODIAC Anth. CO_2 Emission
(b)
EVI
(c)
Vegetation Type
50°N
40°N
30°N
20°N
80°E
90°E
100°E
110°E
120°E
0 2 4 6 8 10 12 14 16 18 20
kmole/km²/h
0 0.1 0.2 0.3 0.4 0.5
Evergreen
Deciduous
Shrubland
Grass
Crop
Other
(d)
(e)

带格式表格

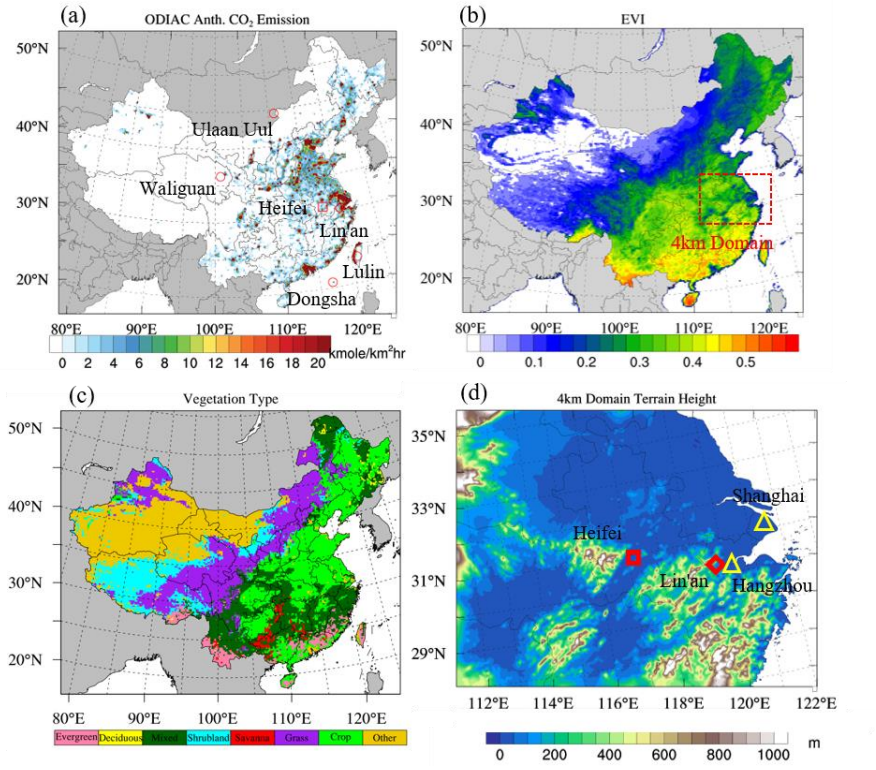

Figure 1: Annual averages of (a) ODIAC emission, (b) MODIS EVI, and (c) dominant vegetation type~~; and (d) photo of Lin'an observation tower; (e) photo of data analysis and recording system~~ in the 20km simulation domain, and (d) terrain height of the 4km simulation domain. The locations of the ESRL sites, TCCON Hefei site, and Lin'an tower site are indicated with red circles, rectangles, and diamonds respectively in (a). The 4km domain is indicated with the red dash rectangle in (b), and the locations of Hangzhou and Shanghai are indicated with yellow triangles in (d).

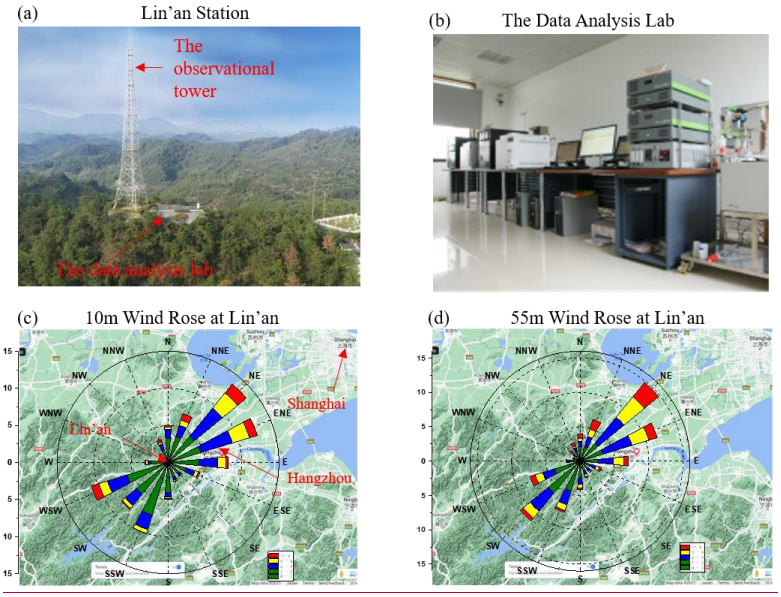

630 **Figure 2: Photos of the (a) Lin'an regional atmospheric background station and (b) the data analysis lab; and wind rose map at Lin'an derived from wind speed and wind direction observations for 2016-2018 at (c) 10m and (d) 50m.**

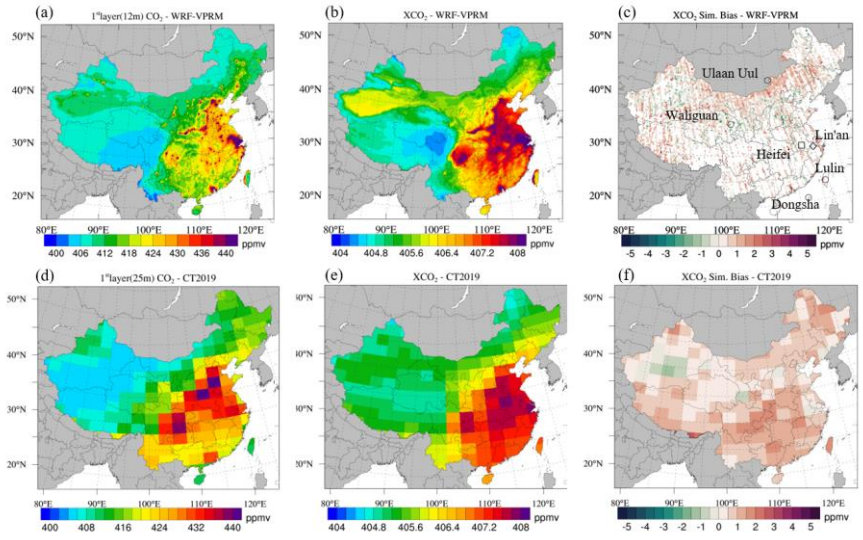
(a)
1st layer(12m) CO2 - WRF-VPRM
(b)
XCO2 - WRF-VPRM
(c)
XCO2 Sim. Bias - WRF-VPRM
Ulaan Uul
Waliguan
Lin'an
Heifei
Lulin
Dongsha
(d)
1st layer(25m) CO2 - CT2019
(e)
XCO2 - CT2019
(f)
XCO2 Sim. Bias - CT2019
50°N
40°N
30°N
20°N
80°E
90°E
100°E
110°E
120°E
400 406 412 418 424 430 436 440
404 404.8 405.6 406.4 407.2 408
-5 -4 -3 -2 -1 0 1 2 3 4 5
400 408 416 424 432 440
ppmv

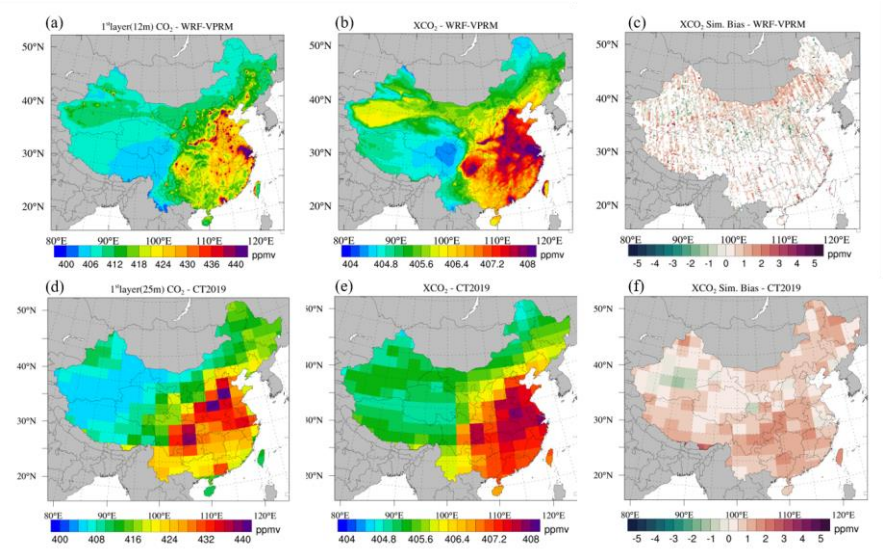

Figure 23: 2016-2018 averages of WRF-VPRM simulations of (a) 1st layer (mid-layer height is 12km) CO_2 concentration, and (b) XCO_2 concentration; (c) WRF-VPRM simulated XCO_2 bias against OCO-2; (d)-(f) is same as (a)-(c) but for CT2019 (1st layer mid-level height is 25m). ~~Markers in (c) represent the locations of ground-based sites.~~

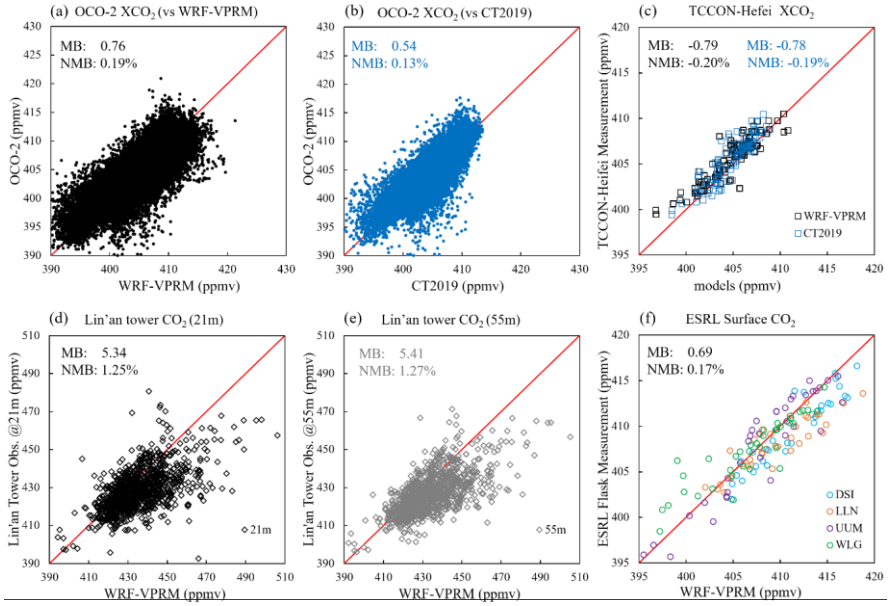
(a) OCO-2 XCO2 (vs WRF-VPRM)
MB: 0.76
NMB: 0.19%
OCO-2 (ppmv)
WRF-VPRM (ppmv)
(b) OCO-2 XCO2 (vs CT2019)
MB: 0.54
NMB: 0.13%
OCO-2 (ppmv)
CT2019 (ppmv)
(c) TCCON-Hefei XCO2
MB: -0.79
NMB: -0.20%
MB: -0.78
NMB: -0.19%
WRF-VPRM
CT2019
TCCON-Heifei Measurement (ppmv)
models (ppmv)
(d) Lin'an tower CO2 (21m)
MB: 5.34
NMB: 1.25%
21m
Lin'an Tower Obs. @21m (ppmv)
WRF-VPRM (ppmv)
(e) Lin'an tower CO2 (55m)
MB: 5.41
NMB: 1.27%
55m
Lin'an Tower Obs. @55m (ppmv)
WRF-VPRM (ppmv)
(f) ESRL Surface CO2
MB: 0.69
NMB: 0.17%
DSI
LLN
UUM
WLG
ESRL Flask Measurement (ppmv)
WRF-VPRM (ppmv)

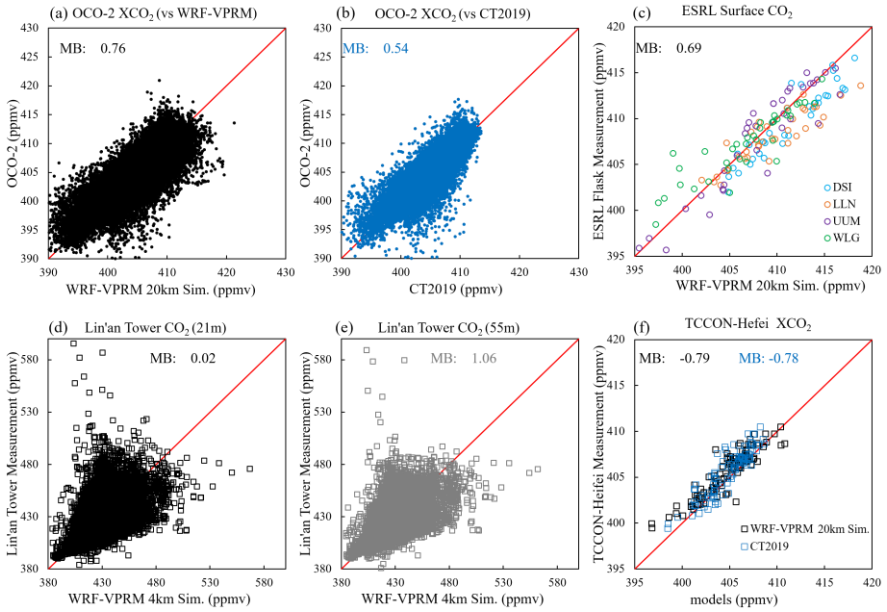

Figure ~~34~~: Data pairs for OCO-2 against (a) WRF-VPRM and (b) CT2019~~,~~; (c) ~~TCCON-Hefei~~ESRL against WRF-VPRM ~~and CT2019,~~; Lin'an tower against WRF-VPRM 4km-grid simulation at (d) 21m and (e) 55m~~,~~; and (f) ~~ESRL~~TCCON-Hefei against WRF-VPRM and CT2019.

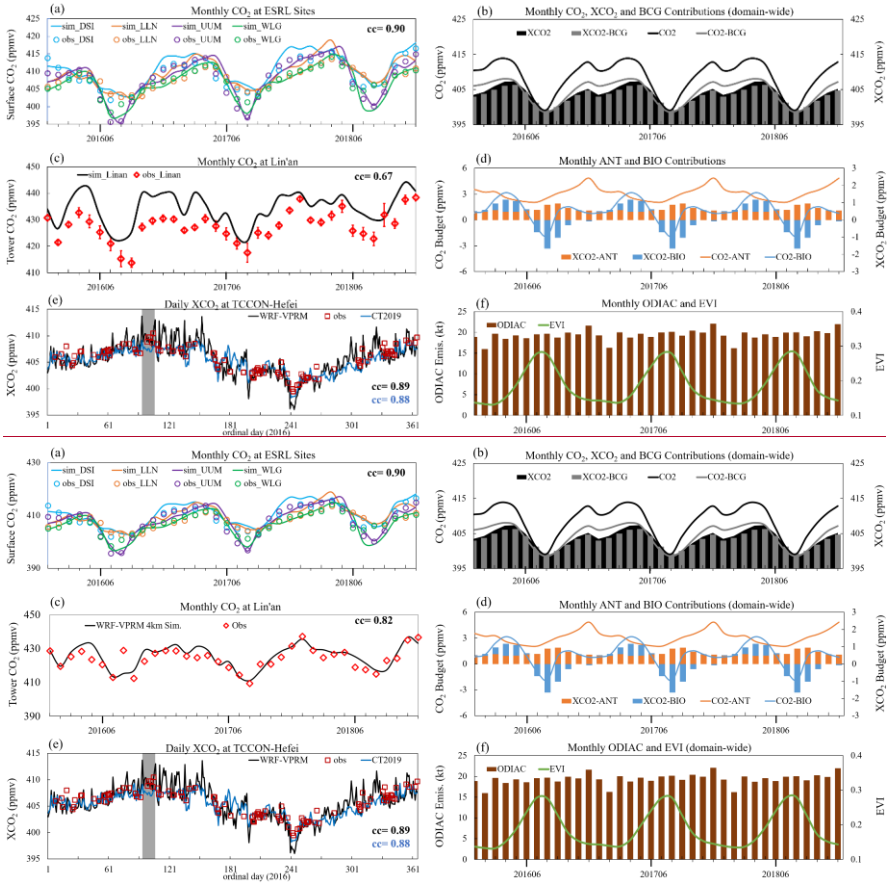

Figure 45: Monthly variations of (a) CO_2 at ESRL sites, (b) total (black) and background (BCG, grey) CO_2 (line) and XCO_2 (area and bar), (c) CO_2 at Lin'an station (averaged for daytime 21m and 55m data); (d) contributions from anthropogenic (ANT, orange) and biogenic (BIO, blue) for CO_2 (lines) and XCO_2 (bars); (f) ODIAC emission and MODIS EVI; and (e) Daily variation of XCO_2 at TCCON-Hefei site.

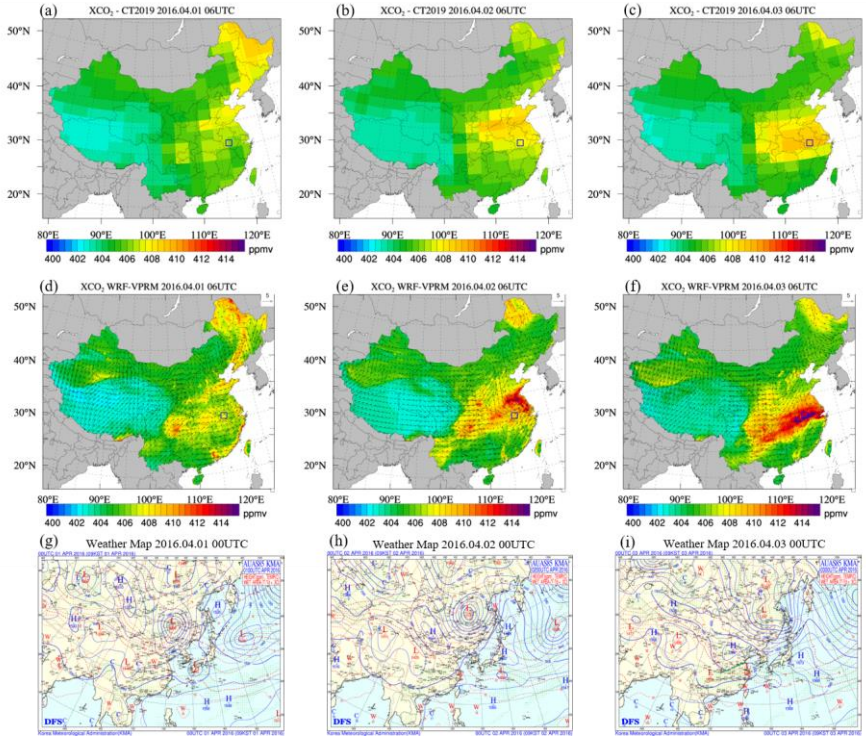

650 **Figure 56: Daily XCO_2 from CT2019 (a-c) and WRF-VPRM (d-f), weather map from Korea Meteorological Administration (g-i). The blue box represents location of Hefei.**

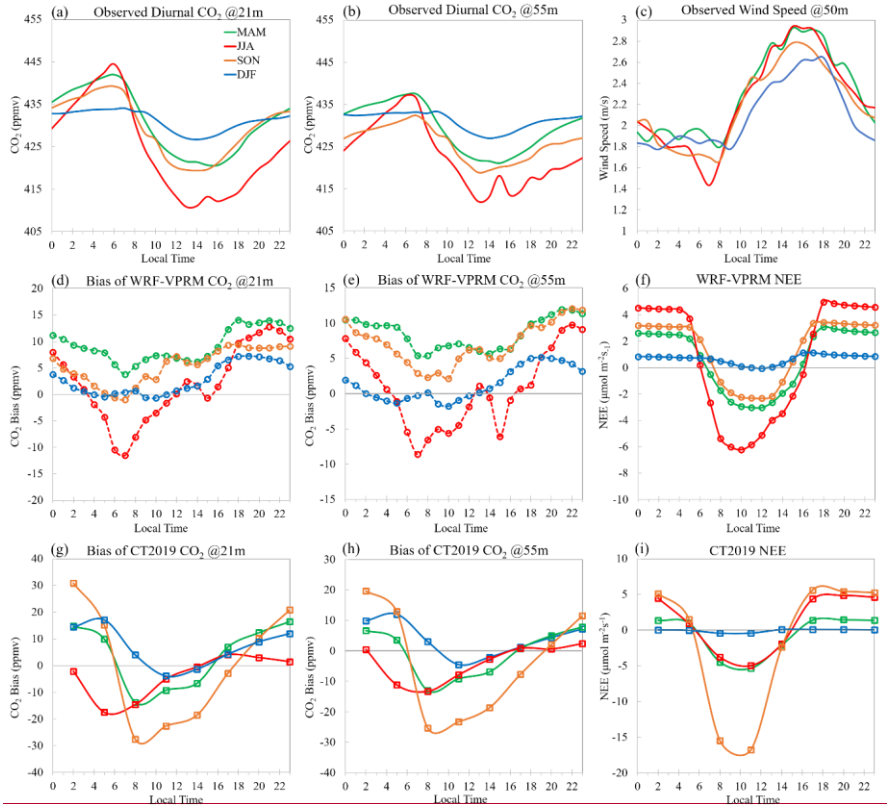
(a) Observed Diurnal CO_2 @21m
MAM
JJA
SON
DJF
(b) Observed Diurnal CO_2 @55m
(c) Observed Wind Speed @50m
(d) Bias of WRF-VPRM CO_2 @21m
(e) Bias of WRF-VPRM CO_2 @55m
(f) WRF-VPRM NEE
(g) Bias of CT2019 CO_2 @21m
(h) Bias of CT2019 CO_2 @55m
(i) CT2019 NEE
CO_2 (ppmv)
CO_2 Bias (ppmv)
Wind Speed (m/s)
NEE (μmol $m^{-2}s^{-1}$)
Local Time

带格式的： 居中

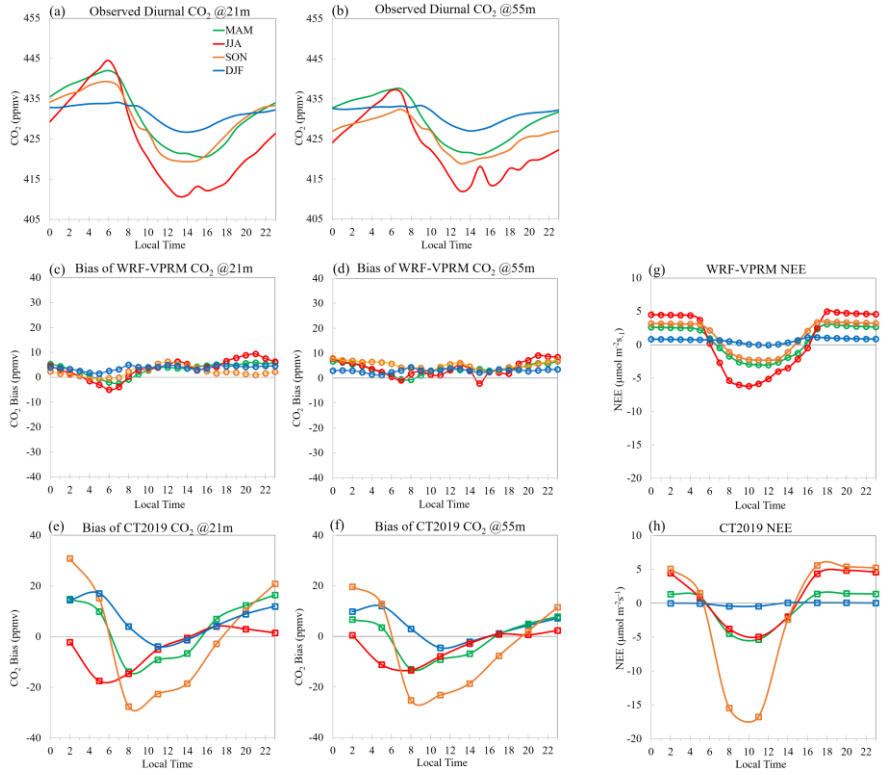

655 **Figure 6~~7~~: Seasonal mean diurnal variations of observed CO_2 at (a) 21m and (b) 55m~~, and (c) wind speed at 50m~~; WRF-VPRM simulation biases of CO_2 at (c) 21m and (d) ~~21m and (e)~~ 55m~~, and (f)~~; CT2019 simulated biases at (e) 21m and (f) 55m; Simulated NEE~~;~~ from (g)~~ (i) are same as (d) (f) but for~~) WRF-VPRM and (h) CT2019.**

带格式的: 字体: 非加粗

带格式的: 两端对齐, 行距: 1.5 倍行距

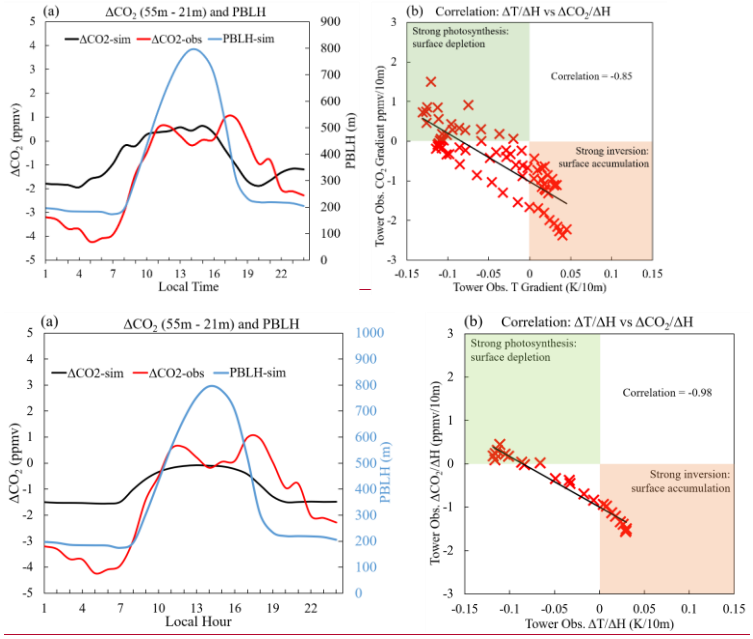

Figure ~~7~~8: (a) Average (2016-2018) diurnal variations of simulated (black line) and observed (red line) ΔCO_2 and simulated (blue line) PBLH at Lin'an station; and (b) correlation between CO_2 gradient between 55m and 21m ($\Delta CO_2/\Delta H$) and temperature gradient ($\Delta T/\Delta H$) at Lin'an station ~~(diurnal data is averaged for each year respectively).~~.

带格式的: 左

带格式的: 左, 行距: 单倍行距